Supercritical CO_2 flow through a layered silica sand/calcite sand system: Experiment and modified Maximal Inscribed Spheres analysis

Timothy J. Kneafsey, Dmitriy Silin, and Jonathan B. Ajo-Franklin
Lawrence Berkeley National Laboratory

Abstract

A core-scale experiment in which supercritical carbon dioxide ($scCO_2$) was flowed through a brine-saturated sample consisting of a layer of silica sand, a layer of calcite sand, and another layer of silica sand from inlet to outlet was performed, and compared to a similar experiment in which nitrogen was flowed through the same sample at the same orientation, effective stress, and temperature. The core-scale experiments were monitored using x-ray computed tomography to examine the flow paths of the fluids. Both nitrogen and $scCO_2$ showed gravity override, however both flowed through a very narrow pathway through the calcite sand, and a broader pathway through the silica sand. Synchrotron computed microtomography volumes were acquired for sub-samples of each type of sand and reconstructions of the sand samples were analyzed using the Maximal Inscribed Spheres method modified for mixed-wet conditions to estimate characteristic curves for a number of contact angles. These characteristic curves are used to explain and interpret the experimental results.

Keywords: wettability, supercritical CO_2, Maximal Inscribed Spheres, X-ray computed tomography, micro-computed tomography

1.0 Introduction

To mitigate the effects of increasing greenhouse gas concentrations in the atmosphere, injection of anthropogenic CO_2 into porous subsurface strata having a confining caprock is being strongly considered and tested in laboratory studies, field pilot studies, and using numerical simulation [*Bachu et al.*, 1994; *Bachu*, 2000; *Bachu and Adams*, 2003; *Bachu and Bennion*, 2008; *Benson et al.*, 2006; *Gunter et al.*, 1993; *Gunter et al.*, 1997; *Holloway and Savage*, 1993; *Holloway and Straaten*, 1995; *Holloway*, 1996; *Holloway*, 2001; *Holloway*, 2007; *Juanes et al.*, 2006; *Kharaka et al.*, 2009; *Kneafsey and Pruess*, 2010; *Oldenburg et al.*, 2001; *Perrin and Benson*, 2010; *Pini et al.*, 2012]. Reservoir rock wettability is of critical importance in predicting flow characteristics of nonaqueous fluids such as gas, oil, organic solvents, and supercritical carbon dioxide ($scCO_2$) through subsurface media [e.g. *Blunt et al.*, 1995; *Chalbaud et al.*, 2009; *Hirasaki*, 1991; *Jung and Wan*, 2012; *Kovscek et al.*, 1993; *Powers and Tamblin*, 1995; *Powers et al.*, 1996; *Soll et al.*, 1993; *Tokunaga*, 2012; *Wilson*, 1994].

How the immiscible fluids occupying a porespace wet the mineral matrix impacts flow through the media dramatically. The wettability directly affects the characteristic curve (capillary pressure-saturation) of the medium, which further impacts the effective permeabilities of the fluids [*Plug and Bruining*, 2007; *Tokunaga*, 2012]. With two fluids present, one will typically be more wetting to the natural surfaces (mineral, organic) than

the other. In most cases, water (or brine) wets reservoir rock preferentially to gas. In oil reservoirs, where oil, brine, and possibly gas are present, the wettability of the mineral matrix is strongly affected by the particular organic compounds present in the oil (e.g asphaltenes), as well as the mineralogy. Many studies have shown that carbonate rock can be more oil wetting than other mineralogies [*Anderson*, 1986]. Measurements of liquid CO_2 contact angles on crystalline calcite at room temperature have shown low contact angles, similar to the liquid CO_2 contact angle on clean flat glass [*Espinoza and Santamarina*, 2010]. Significant contact angles were observed in the CO2 - brine – silica system [*Kim et al.*, 2012].

When a nonwetting fluid is introduced into a mineral medium saturated by the wetting fluid, several cases are important. Where the driving force of the nonwetting fluid is high (high capillary number), such as near an injection well, the nonwetting fluid will displace much of the wetting fluid (plug flow type behavior) because the capillary forces are overcome by the viscous driving force. Farther away from a well, however, capillary forces will cause the nonwetting fluid to preferentially flow in and occupy the larger pores and fractures (low capillary number, capillary fingering) [e.g. Lenormand et al., 1988]. This is not ideal for the case of injecting $scCO_2$ into a preferentially brine-wetting reservoir, as it will tend to reduce the relative volume of CO_2 that can be injected. The radial distance from a well at which the transition between high capillary number and low capillary number flow is dependent on the specific conditions of the injection scenario (e.g. injection rate, porosity, and reservoir thickness); however, for a typical geologic carbon sequestration scenario, it can occur quite close to the well bore, on the order of 10-20 m, dramatically influencing reservoir storage capacity.

To investigate how $scCO_2$ would flow through rocks of different wettability (to oil), we performed an experiment where $scCO_2$ was flowed through a brine saturated sample composed of a layer of silica sand, a layer of calcite sand, and another layer of silica sand. We imaged the experiment using x-ray computed tomography to determine the flow pathways. To provide a standard for comparison, we first flowed nitrogen through the same brine-saturated sample at the same temperature, orientation, and effective stress. Our hypothesis was that nitrogen would be nonwetting to both minerals, and based on carbonates tending to be more oil wetting, the CO_2 would be partially wetting to the silica, and CO_2 would be more wetting of the calcite than silica, although this turned out to be incorrect.

To provide a tool to understand the test, we imaged the porespace of the two sands using synchrotron computed micro-tomography (microCT). Using the three dimensional description of the porespace extracted from segmented microCT images, we applied the Maximal Inscribed Spheres (MIS) method [*Benson et al.*, 2006; *Silin et al.*, 2010; *Tomutsa et al.*, 2007] modified to incorporate mixed wettability and computed characteristic curves for the sands for various contact angles. The combination of techniques – core scale experiment with imaging, microCT imaging of the porespace, and the use of Maximal Inscribed Spheres provides a powerful multi-scale toolset for physical understanding of flow behavior in porous media.

2.0 Method

2.1 Core-Scale Experiment

Silica sand (F110, US Silica) with roundness 0.710 was sieved and the fraction from 125 to 177 microns was washed with distilled water to remove fines. The 75 to 150 micron fraction of calcite sand with grain roundness 0.705 (Big Brand Water Filter, calcite verified by X-ray diffraction) was similarly washed to remove fines (Figure 1). The slightly smaller grain size for the calcite sand was selected to test wettability on the calcite. If the CO_2 were not wetting to the calcite, we anticipated that the boundary between the coarser silica sand and the slightly finer calcite sand would provide a capillary barrier inhibiting flow into the calcite. If the CO_2 were wetting to the calcite, the finer calcite sand would preferentially imbibe the CO_2.

A 5.08 cm inside diameter elastomer (ethylene propylene diene) sleeve was attached to a 5.08 diameter polyvinyl chloride (PVC) endpiece with a 6 mm hole in the center containing a 2 mm thick 316L stainless steel frit (Mott Corporation, Farmington, CT, USA). The sands were packed dry in approximately 1 cm lifts tamping each layer 60 times with a 2.5 cm diameter 0.5 kg rod. After about one third of the sample volume was filled with the silica sand, calcite sand was placed in the sleeve the same way. When about 2/3 of the volume was filled, silica sand was placed in the sleeve resulting in a sandwiched silica sand/calcite sand/silica sand layered sample (Figure 2). When the elastomer sleeve was filled to the appropriate level with sand, a matching PVC endpiece with a stainless steel frit was placed over the sample and sealed to the sleeve. When assembling the sample, four small pieces of brass wire were emplaced between the silica sand and calcite sand layers to allow easy identification of the layers by x-ray computed tomography. The dimensions of the layers were measured and the mass of sand in each layer quantified to allow calculation of the porosity (Table 1). The assembly was then submerged in confining fluid (propylene glycol/water mix) in an X-ray transparent pressure vessel and confining stress was applied to the outside of the elastomer sleeve.

The pressure vessel was mounted to the table of a modified Siemens Somatom HiQ medical CT scanner, and associated tubing was connected (Figure 2). Fluid from a circulating temperature bath was used to control the temperature of the sample to 46.7 C± 0.5 C, as indicated by a thermocouple located inside the pressure vessel taped to the outside of the elastomer sleeve. Fluids were pumped using high-pressure syringe pumps (Teledyne ISCO).

After mounting the vessel to the CT scanner table, the effective stress (confining pressure around the sample minus the pore pressure) was maintained at 1.38 MPa ± 0.46 MPa (when raising or lowering pressure) with tests performed at a 1.38 MPa effective stress. The dry sample was CT scanned to provide baseline sample density. At the beginning of the test sequence, the sand sample was evacuated using a vacuum pump and then filled with 5 molar NaCl brine. This brine was used because Kim et al. (2012) found that this concentration has a large effect on the CO_2-brine contact angle in silicamicromodel observations .

The test sequence was as follows:

1. Establish 1.38 MPa effective stress on the dry sample and CT scan
2. Evacuate, saturate with 5 M NaCl brine, and CT scan
3. Flow several pore volumes of brine at 0.35 ml/min and 1.38 MPa pore pressure
4. Nitrogen Flood - Flow nitrogen (1.38 MPa pore pressure) at 0.5 ml/min with intermittent stops for CT scanning, using downstream syringe pump to control rate
5. Upon nitrogen breakthrough, flow ~2 pore volumes of brine at 1 ml/min (nominal pore velocity ~ 2 m/day) and CT scan
6. Lower pore pressure (and confining pressure maintaining 1.38 MPa effective stress) to low value using vacuum pump, then resaturate with brine to 8.28 MPa
7. Flow several pore volumes of brine at 0.3 ml/min
8. CO_2 Flood - Flow CO_2 at 8.28 MPa at 0.5 ml/min using downstream syringe pump to control rate, periodically stopping flow to CT scan
9. Following CO_2 breakthrough, flow ~2 pore volumes of brine and then CT scan
10. Dry sample (18 pore volumes of water to remove salt, 3 pore volumes CO_2 saturated methanol, dry gas flow until constant density reached by CT) and CT scan

Properties of the fluids used in this experiment are listed in Table 2. The density of the $scCO_2$ used in this test is lower by a factor of two or more than the density of $scCO_2$ at current and planned field test sites, but corresponds with the scCO2 density in experiments performed by Kim et al. (2012).

2.2 MicroCT Characterization

Samples of the silica and calcite sands were placed in thin-walled 6061 aluminum tubes with an outer diameter of ~3 mm and scanned at the synchrotron microCT facility (Beamline 8.3.2, http://microct.lbl.gov/) at the Advanced Light Source, Lawrence Berkeley National Laboratory. Details of the synchrotron micro-tomography technique can be found in *Stock* (2009); experimental studies discussing the current acquisition environment at Beamline 8.3.2 can also be found in the literature (e.g. [*Armstrong and Ajo-Franklin*, 2011; *Noiriel et al.*, 2012; *Silin et al.*, 2010]). Scans were conducted using a multilayer monochromator (set at 26 KeV), a 1 mm cadmium tungstate scintillator ($CdWO_4$), and a cooled high resolution CCD detector (PCO Edge, 2560 x 2160). Each scan consisted of 1800 projections (0.1 degree spacing); with the selected optics, the reconstructed volumes were sampled at a voxel size of 3.3085 microns. An example of single slices from both the silica and calcite image volumes is shown in Figure 3; note the similar grain morphologies with the calcite sand exhibiting slightly rougher surfaces and higher apparent x-ray attenuation (brighter). After acquisition, the image volumes were de-noised and segmented in preparation for MIS modeling. An example of the processed microCT volumes is shown in Figure 4 with MIS computed saturations for two contact angles (details to follow).

3.0 Results

3.1 Core-Scale Experiment

Our sample is depicted in figures here as a series of circular cross sections imaged by the CT scanner. Each figure consists of a series of images of 3 mm thick circular cross sections (slices), with the top left being near the injection location, continuing left to right and top to bottom until reaching the slice closest to the exit rightmost on the bottom row. In the first slice in Figure 5a, it is possible to see a portion of the pattern machined into the endcaps to aid in fluid distribution over the surface. Figure 5a shows the distribution of slices having silica sand and calcite sand. Because of the density difference between the minerals, they are easily distinguishable by CT. In this paper, the first two rows of all figures showing CT results are of the upstream silica sand, the middle two rows are of the calcite sand, and the lower two rows are of the downstream silica sand. The first slice shown in the third and fifth rows show transition between layers. Nitrogen saturation computed from CT scans following breakthrough is shown in Figure 5b, and the CO_2 saturation following breakthrough is shown in Figure 5c.

In the region near the injection point, nitrogen displaced much of the brine (first ~four slices) before the effect of gravity override dominated downstream of that. In the CO_2 flood, CO_2 displaced less brine in the silica sand near the entry point than nitrogen, but formed a thicker more saturated layer at the top. In the calcite sand zone, both invading fluids (nitrogen and CO_2) flowed in a narrow region along the top arc of the sample and did not penetrate as far into the calcite sand as they did into the silica sand. In the downstream silica sand, the flow pattern returned to be similar to that in the upstream silica sand, but through a smaller cross section. Average saturation profiles of nitrogen or CO_2 saturation taken along a vertical line for slices having similar saturations over about 3 cm (2.7 to 3.6 cm) thicknesses along the sample axis are shown in Figure 6. These profiles were taken along the line shown in the inset in Figure 6a.

Figure 7 shows the difference between the final invading phase saturations for the two cases with higher CO_2 saturation shown in red and higher N_2 saturation shown in blue. It is clear that the invasion patterns were similar for the two invading phases, but not identical, with higher nitrogen saturation (blue) near the inlet, higher CO_2 saturation and greater extent downstream in the inlet-side silica sand, higher CO_2 saturation and greater extent in the calcite sand, and higher N_2 saturation and extent in the downstream silica sand.

The nitrogen and CO_2 phase saturations remaining following ~ 2 pore volume (pv) brine flood (2.31 pv for nitrogen and 2.07 pv for CO_2) are shown in Figure 8, and Figure 9 shows saturation profiles along the same line shown in Figure 6a. In the case of nitrogen, the gas saturation was reduced from about 50% to about 20% throughout the upstream and downstream silica sand regions that had previously contained nitrogen. The calcite sand did not originally contain much nitrogen, and the nitrogen appears to have been completely flushed from the calcite within the limits of the observation. In the case of CO_2, residual CO_2 was only apparent in the downstream silica sand. Slight negative values for the CO_2 saturations in the calcite sand result from some consolidation of the calcite over the test duration.

3.2 Analysis - Maximal Inscribed Spheres

The method of maximal inscribed spheres technique (MIS) [Silin and Patzek, 2006, Silin et al., 2003, Silin, *et al*., 2010, and Section 5 of Silin, 2012] employs the one-to-one correspondence between the magnitude of the capillary pressure and the mean curvature of the interface between two immiscible fluids in equilibrium. Given a segmented image of the pore space, the MIS algorithms calculate the volume occupied by the nonwetting fluid through inscribing spheres of a given radius and testing the connectivity of the obtained structure. The radius is derived from the magnitude of capillary pressure through the Young-Laplace equation. Plotting the capillary pressure versus relative pore volume complementary to the volume covered by the spheres yields an estimate of capillary pressure as a function of saturation. Different connectivity concepts make it possible to model drainage or imbibition of two-phase fluid distributions. Although MIS calculations treat the fluid-fluid interface curvature in a simplified way, the outcome is in agreement with experimental results, both in micro- and macro-scales.

The MIS technique modified to incorporate contact angle, [see Section 2 in Silin et al., 2012], was used to compute characteristic curves for the two sands from segmented images from microCT analysis assuming different contact angles. Figure 10 shows plots of capillary pressure curves evaluated for calcite and silica sand packs. The computed curves are dimensionless and only reflect the shapes and sizes of the pores. To be physically meaningful, the plots have to be scaled by a factor equal to the ratio of the interfacial tension coefficient to the physical voxel size. At zero contact angle, the computed P_c curves for silica and calcite sands almost coincide, indicating that the grain shapes and sizes are similar in both packs.

In a horizontal core, buoyancy segregates gas and brine. The flow rate in the experiments was small (nominally 1 m/day for the invading fluid floods), so that we assume that the capillary pressure is determined by saturation:

$$P_c = P_c(S) \tag{1}$$

where S denotes brine saturation.
The hydrostatic pressure gradient is different for gas and brine, thus

$$P_c(S(z)) = P_c(S(z_{\text{ref}})) + (\tilde{n}_g - \tilde{n}_w) g (z - z_{\text{ref}}) \tag{2}$$

Here z is the vertical coordinate, $\tilde{n}_g$ and $\tilde{n}_w$ are gas and brine densities, and g is gravity acceleration.
It is difficult to achieve an ideally homogeneous grain pack. The grains are packed less densely near the isolating sleeve boundary. Thus, we introduce a correction factor $f(r)$, which is equal to one near the center of the core, and is less than one near the sleeve. The saturation evaluated in CT scan satisfies equation:

$$J(S(x,z)) = \frac{d}{\sigma} \frac{P_c(S(z_{\text{ref}})) + (\tilde{n}_g - \tilde{n}_w) g (z - z_{\text{ref}})}{f(r)} \tag{3}$$

The distance to the axis of the core, r, can be expressed through x and z:

$$r(x,z)^2 = x^2 + (z - z_0)^2 \tag{4}$$

In the last equation, the coordinates of the horizontal core axis are $x = 0$ and $z = z_0$.

Figure 11 shows two saturation patterns calculated for a vertical slice of a horizontal cylindrical core. The color bars show gas saturation. The result shown in Figure 11a is obtained assuming no packing effect, whereas in the Figure 11b the packing effect is modeled with a distribution $f(r)$ defined by equation

$$f(r) = \frac{1}{1 + 0.1 \max\left\{2r - 1, 0\right\}^4} \tag{5}$$

A comparison of Figure 11 to the saturation patterns in Figure 5 qualitatively confirms the presence of packing effect mentioned above.

Figure 4 shows the calculated capillary equilibrium gas-brine distribution computed using MIS for a micro-CT image volume of the calcite sand pack. The lightest color denotes volume occupied by gas, the darkest color corresponds to solid grains, and the intermediate gray denotes brine. The estimated saturation in both images (a) and (b) is near 48 %. The ordinary percolation calculations model fluid distribution without accounting for connectivity. This is why both images (a) and (b) show some disconnected gas ganglia. An MIS simulation such as this is better suited to simulate gas coming out of the solution or liquid dropout at a dewpoint, but not a displacement of one fluid by the other. A comparison between Figure 4(a) and Figure 4(b) suggests that the gas phase is better connected for contact angle of 60° than for zero contact angle, whereas the curvature of disconnected gas bubbles is smaller.

Figure 12 shows gas saturation distribution in the core evaluated for zero (a) and 20° (b) contact angles. The core-scale simulations were performed assuming ρ_w=1181 kg/m^3, ρ_g =263 kg/m^3, and considering the packing effect model defined in Eq. (5). The capillary pressures were computed from the calcite invasion simulations shown in Figure 4 scaled by voxel size of 3.31 μm and interfacial tension coefficient $\sigma = 46 \times 10^{-3}$ N/m, see [*Bachu and Bennion*, 2008; *Kim et al.*, 2012]. The simulation shows that fluid distribution is sensitive to the contact angle. Contact angles of zero and 20º resulted in simulation results that can be compared with the experimental results, with the 0º (nonwetting) comparing nicely with the CO_2 flood in the calcite sand, and the 20º contact angle results comparing favorably with the CO_2 flood in the silica sand.

4.0 Discussion

Micromodel examinations of $scCO_2$ in brine-wet fused silica showed increasing contact angle with increasing brine ionic strength, and nonuniform contact angles in a very homogeneous and relatively pure system [*Kim et al.*, 2012]. Our system was different in that our silica sand is a natural sand with surface roughness and contains a variety of grain shapes and some variation in grain size (Figure 1) resulting in a heterogeneous pore structure. This pore structure was further complicated by packing artifacts indicated by higher porosity near the elastomer sleeve. Our calcite sand is crushed calcite, has rough surfaces, and the grains appear slightly more angular than the silica sand. Surface roughness and impurities in natural media could affect behavior of the invading fluids [*Spori et al.*, 2008].

Both invading fluids penetrated deeper into the silica sand than the calcite sand. This could be due to the different wetting properties of the two mineral media, and/or from the smaller pore size in the calcite sand causing a capillary barrier to form. Kim et al. (2012) saw only small contact angles for the gas/brine/fused silica system; similarly we would expect that the nitrogen would act as a nonwetting fluid relative to the brine. If we assume the CO_2 behaves the same in our system on the silica grains as the fused silica system of Kim et al, (2012), we would expect some invasion of the CO_2 into the silica sand beyond that of the nitrogen because of the non-zero contact angle (up to ~ 75º in their study, ~20º in [*Jung and Wan*, 2012], perhaps ~20º in this study). Figure 6 shows this greater invasion in both the inlet silica sand and to some extent in the calcite sand.

In the downstream silica sand, the nitrogen penetrates deeper than the CO_2. The porosity of the downstream silica sand is the highest in the system. It is not clear why the CO_2 does not penetrate as far as the N_2 here. If a source of contamination were present (e.g. elastomer dissolution by $scCO_2$ or dissolution of some residual organic compounds not removed by system cleaning), this would tend to reduce the interfacial tension. This would likely result in greater rather than less invasion. The effect of CO_2 dissolution into the brine would occur throughout the sample and not only the final section, indicating that dissolution is probably not the cause. A potential cause could be that the system changed slightly over the duration of the tests. The calcite sand consolidated somewhat over the test indicating mineral dissolution and precipitation occurred. It is not known when the consolidation occurred, but the dried calcite sand was recovered in a clump, whereas the silica sand flowed out as it flowed in. It is possible that some calcite dissolution and precipitation occurred, and precipitated calcite on the downstream silica sand altered its wettability towards the more brine-wetting calcite. Depending on the amount of precipitation, this might also affect the pore geometry, making pores smaller and further reducing the distance that CO2 would penetrate. Neither optical microscopy nor scanning electron microscopy with energy dispersive spectroscopy showed the presence of calcite precipitate, however, the sampling of the sand was very coarse because a refined examination of the sample was not planned.

The brine flood that followed the N_2 or CO_2 floods reduced the N_2 and CO_2 saturations at the outlet end of the column to about 20%. From the inlet through the inlet silica sand and the calcite sand, the CO_2 saturation was reduced to below detection using the CT data. This is because the CO_2 is displaced by the brine, and dissolved into the passing brine. Under the experimental conditions, the equilibrium CO_2 mole fraction is 0.73E-02, which is equivalent to 0.48 molal [calculated using *Spycher and Pruess*, 2010]. Following the CO_2 flood, approximately 1.85 g CO_2 was present in the sample, and a maximum of 4.2 g could be removed from the system by dissolution into the 2 pore volumes of brine. Nitrogen is far less soluble than CO_2 under the experimental conditions, thus dissolution was not as significant.

Common elements present in both the nitrogen and CO_2 floods include the circular region near the outer sample radii where invasion occurs. This indicates a packing difference at that location, likely having a slightly higher porosity, larger pores, and a higher permeability. This was not easily seen in the CT data, however at the sample outer radii

beam hardening from a polychromatic x-ray source (softer x-rays being more strongly attenuated than harder x-rays), and contrast artifacts at discrete borders resulting from tomographic reconstruction artifacts can increase the difficulty in interpreting this information. There is a clear capillary barrier between the silica and calcite sands.

Our system contained materials other than silica and calcite including PVC endcaps, multiple metals (Nitronix 50, 316 stainless steel, 304 stainless steel), Teflon seals, and also the elastomer sleeve. Although this experiment was intended to investigate the difference in flow behavior between silica and calcite, the effect of the elastomer sleeve material should also be considered because gravity override caused both CO_2 and nitrogen to flow near or in contact with it. The wettability of the elastomer sleeve was not measured. If the sleeve were invading-fluid wetting, the sleeve would tend to guide the invading fluid along it (See Figure 2 in [*McBride et al.*, 1992]). One might also expect a more porous (and permeable) layer at the elastomer/sand boundary because of packing. Next to a rigid surface, such a layer would be expected [*Ransohoff and Radke*, 1988]. This concept is complicated, however, by the effect of the confining pressure forcing the flexible sleeve into the sand, resulting in a sandpaper-like surface. Indeed, sleeves removed from tests (including this test) generally have the grain structure impressed on their inside surface and sand grains lining the elastomer. Because the invading fluids do not only flow across the very top layer, particularly in the silica sand, we acknowledge that there could be an effect, but base our observations on flow away from the sleeve. An experimental approach that might eliminate this possible influence would be to use a elastomer sleeve possibly lined with a layer of nickel to reduce CO_2 absorption by the elastomer, and Teflon to provide a soft contact with the sand [*Pini et al.*, 2012], further lined with a fine nonreactive water-wetting material such as cloth. Assembling this system would be quite complicated however.

5.0 Conclusions

We performed a laboratory experiment in which $scCO_2$ and N_2 were individually flowed through a layered silica sand/calcite sand/silica sand sample and imaged the resulting flow characteristics using x-ray CT. We created a model porespace for our sands using synchrotron microCT imaging, and computed characteristic curves for our media for a range of contact angles using the method of Maximal Inscribed Spheres. We applied these characteristic curves to our observations and accounted for a systematic sand packing artifact, and provided simple equilibrium-based comparisons to our observations.

Simple physical arguments and analysis using MIS indicate that CO_2 is not wetting to calcite under the experimental conditions and duration. The computations performed using MIS, when a packing artifact model is considered, were able to match the observations qualitatively. The CO_2 was not actively imbibed into the calcite (or the silica). This is in agreement with room temperature results from Espinoza and Santamarina (2010), who also indicate that large changes in the contact angle are not expected with increasing pressure (examined by Jung and Wan (2012)). Our experimental duration was too short to allow for an explicit examination of chemical effects (dissolution and precipitation associated with CO_2 presence) on wettability, although we perhaps observed an effect of this. We purposely did not expose the sample to CO_2 prior

to the nitrogen flood to avoid contact angle changes which may occur resulting from scCO2 penetration into the silica [*Bikkina*, 2011; *Chalbaud et al.*, 2009; *McCool and Tripp*, 2005]. These changes may occur in natural systems or tests over a longer duration, and longer duration tests are needed to understand these effects.

In our experiment, calcite sand tended to be brine wetting, and perhaps more brine wetting than silica sand. Because of the grain size differences, we cannot conclusively compare wettabilities of the fluids on these sand surfaces.

6.0 Acknowledgements

This work was performed at Lawrence Berkeley National Laboratory (LBNL) of the U.S. Department of Energy (DOE) under Contract No. DE-AC02-05CH11231. Synchrotron microtomography was performed at the Advanced Light Source at LBNL, Beamline 8.3.2 under Approved Program ALS-05061, which is supported by the Office of Science, Office of Basic Energy Sciences, U. S. DOE under Contract No. DE-AC02-05CH11231 with the assistance of Alastair MacDowell and Dula Parkinson. J. Ajo-Franklin was supported by the Center for Nanoscale Control of Geologic CO_2, an Energy Frontier Research Center funded by the U.S. Department of Energy, Office of Science, Office of Basic Energy Sciences under Award Number DE-AC02-05CH11231. X-ray diffraction analysis of the calcite was performed by Jonathan Icenhower and SEM/EDS observations were performed by Marco Voltolini.

7.0 References

Anderson, W. G. (1986), Wettability Literature Survey-Part 1: Rock/Oil/Brine Interactions and the Effects of Core Handling on Wettability, *Journal of Petroleum Technology* (October), 1125-1144.

Argaud, M. J. (1993), Predicting the interfacial tension of brine/gas (or condensates) systems, in *Advances in Core Evaluation III Reservoir Management*, edited by P. F. Worthington, p. 496, Taylor and Francis.

Armstrong, R., and J. Ajo-Franklin (2011), Investigating biomineralization using synchrotron based X-ray computed microtomography, *Geophys. Res. Lett.*, *38*(8), L08406.

Bachu, S., et al. (1994), Aquifer disposal of CO_2: Hydrodynamic and mineral trapping, *Energy Conversion and Management*, *35*(4), 269-279.

Bachu, S. (2000), Sequestration of CO_2 in geological media: criteria and approach for site selection in response to climate change, *Energy Conversion and Management*, *41*(9), 953-970.

Bachu, S., and J. J. Adams (2003), Sequestration of CO_2 in geological media in response to climate change: capacity of deep saline aquifers to sequester CO_2 in solution, *Energy Conversion and Management*, *44*(20), 3151-3175.

Bachu, S., and D. B. Bennion (2008), Interfacial Tension between CO_2, Freshwater, and Brine in the Range of Pressure from (2 to 27) MPa, Temperature from (20 to 125) C, and Water Salinity from (0 to 334,000) mg/L, *Journal of Chemical & Engineering Data*, *54*(3), 765-775.

Benson, S. M., et al. (2006), Core scale and pore scale studies of carbon dioxide migration in saline formations, in *8th International Conference on Greenhouse Gas Control Technologies*, edited.

Bikkina, P. K. (2011), Contact angle measurements of CO_2-water-quartz/calcite systems in the perspective of carbon sequestration, *International Journal of Greenhouse Gas Control*, *5*(5), 1259-1271.

Blunt, M., et al. (1995), Three-phase flow and gravity drainage in porous media, *Transport in Porous Media*, *20*(1/2), 77-103.

Chalbaud, C., et al. (2009), Interfacial tension measurements and wettability evaluation for geological CO_2 storage, *Advances in Water Resources*, *32*(1), 98-109.

Espinoza, D. N., and J. C. Santamarina (2010), Water-CO_2-mineral systems: Interfacial tension, contact angle, and diffusion-Implications to CO_2 geological storage, *Water Resour. Res.*, *46*(7), W07537.

Gunter, W. D., et al. (1993), Aquifer Disposal of CO_2-Rich Gases: Reaction Design for Added Capacity, *Energy Conversion Management*, *34*(9-11), 941-948.

Gunter, W. D., et al. (1997), Aquifer disposal of CO_2-rich greenhouse gases: extension of the time scale of experiment for CO_2-sequestering reactions by geochemical modelling, *Mineralogy and Petrology*, *59*, 121-140.

Hirasaki, G. J. (1991), Wettability: Fundamentals and Surface Forces, *SPE Formation Evaluation*, *June 1991*, 217-226.

Holloway, S., and D. Savage (1993), The Potential for Aquifer Disposal of Carbon Dioxide in the UK, *Energy Conversion Management*, *34*(9-11), 925-932.

Holloway, S., and R. v. d. Straaten (1995), The Joule II Project The Underground Disposal of Carbon Dioxide, *Energy Conversion Management*, *36*(6-9), 519-522.

Holloway, S. (1996), An Overview of the Joule II Project 'The Underground Disposal of Carbon Dioxide', *Energy Conversion Management*, *37*(6-8), 1149-1154.

Holloway, S. (2001), Storage of fossil fuel-derived carbon dioxide beneath the surface of the Earth, *Annual Review of Energy and Environment*, *26*, 145-166.

Holloway, S. (2007), Carbon dioxide capture and geological storage, *Philosophical Transactions of the Royal Society A: Mathematical, Physical and Engineering Sciences*, *365*(1853), 1095-1107.

Juanes, R., et al. (2006), Impact of relative permeability hysteresis on geological CO_2 storage, *Water Resour. Res.*, *42*(12), W12418.

Jung, J.-W., and J. Wan (2012), Supercritical CO_2 and Ionic Strength Effects on Wettability of Silica Surfaces: Equilibrium Contact Angle Measurements, *Energy & Fuels*.

Kharaka, Y. K., et al. (2009), Potential environmental issues of CO_2 storage in deep saline aquifers: Geochemical results from the Frio-I Brine Pilot test, Texas, USA, *Applied Geochemistry*, *24*(6), 1106-1112.

Kim, Y., et al. (2012), Dewetting of Silica Surfaces upon Reactions with Supercritical CO2 and Brine: Pore-Scale Studies in Micromodels, *ES&T*, *46*(7), 4228.

Kneafsey, T., and K. Pruess (2010), Laboratory Flow Experiments for Visualizing Carbon Dioxide-Induced, Density-Driven Brine Convection, *Transport in Porous Media*, *82*(1), 123-139.

Kovscek, A. R., et al. (1993), A Pore-Level Scenario for the Development of Mixed Wettability in Oil Reservoirs, *AIChE Journal*, *39*(6), 1072-1085.

Lemmon, E. W., et al. (2012), Thermophysical Properties of Fluid Systems, in *NIST Chemistry WebBook, NIST Standard Reference Database Number 69*, edited by P. J. Linstrom and W. G. Mallard, National Institute of Standards and Technology, Gaithersburg MD, 20899, http://webbook.nist.gov, (retrieved July 9, 2012).

Lenormand, R., et al. (1988), Numerical models and experiments on immiscible displacements in porous media, *Journal of Fluid Mechanics*, *189*, 165-187.

McBride, J. F., et al. (1992), Interfacial Spreading Effects on One-Dimensional Organic Liquid Imbibition in Water-Wetted Porous Media, *Journal of Contaminant Hydrology*, *11*, 1-25.

McCool, B., and C. P. Tripp (2005), Inaccessible Hydroxyl Groups on Silica Are Accessible in Supercritical CO_2, *The Journal of Physical Chemistry B*, *109*(18), 8914-8919.

Noiriel, C., et al. (2012), Upscaling calcium carbonate precipitation rates from pore to continuum scale, *Chemical Geology*, *318-319*, 60-74.

Oldenburg, C. M., et al. (2001), Process Modeling of CO_2 Injection into Natural Gas Reservoirs for Carbon Sequestration and Enhanced Gas Recovery, *Energy & Fuels*, *15*(2), 293-298.

Perrin, J.-C., and S. Benson (2010), An Experimental Study on the Influence of Sub-Core Scale Heterogeneities on CO_2; Distribution in Reservoir Rocks, *Transport in Porous Media*, *82*(1), 93-109.

Pini, R., et al. (2012), Capillary pressure and heterogeneity for the CO_2/water system in sandstone rocks at reservoir conditions, *Advances in Water Resources*, *38*(0), 48-59.

Plug, W. J., and J. Bruining (2007), Capillary pressure for the sand,CO_2,water system under various pressure conditions. Application to CO_2 sequestration, *Advances in Water Resources*, *30*(11), 2339-2353.

Powers, S. E., and M. E. Tamblin (1995), Wettability of Porous Media after Exposure to Synthetic Gasolines, *Journal of Contaminant Hydrology*, *19*, 105-125.

Powers, S. E., et al. (1996), Wettability of NAPL-Contaminated Sands, *Journal of Environmental Engineering*, *122*(10), 889-896.

Ransohoff, T. C., and C. J. Radke (1988), Mechanisms of Foam Generation in Glass-Bead Packs, *SPE Reservoir Engineering*(May), 573-585.

Silin, D.B. and T. Patzek (2006), Pore space morphology analysis using maximal inscribed spheres, *Physica A. Statistical Mechanics and its Applications* 371, 336–360.

Silin D.B., et al., (2003), Robust determination of the pore-space morphology in sedimentary rocks, SPE 84296, 2003 SPE Annual Technical Conference and Exhibition, Denver, Colorado, U.S.A., SPE.

Silin, D. (2012), Digital Rock Studies of Tight Porous Media, LBNL Report 5809E.

Silin, D., et al. (2012), Pore-Scale Study of the Impact of Fracture and Wettability on Two-Phase Flow Properties of Rock", LBNL report 5810E.

Silin, D., et al. (2010), Microtomography and Pore-Scale Modeling of Two-Phase Fluid Distribution, *Transport in Porous Media*, 1-21.

Soll, W. E., et al. (1993), Micromodel Studies of Three-Fluid Porous Media Systems: Pore-Scale Processes Relating to Capillary Pressure-Saturation Relationships, *Water Resources Research*, *29*(9), 2963-2974.

Spori, D. M., et al. (2008), Beyond the Lotus Effect: Roughness Influences on Wetting over a Wide Surface-Energy Range, *Langmuir*, *24*(10), 5411-5417.
Spycher, N., and K. Pruess (2010), A Phase-Partitioning Model for CO2–Brine Mixtures at Elevated Temperatures and Pressures: Application to CO2-Enhanced Geothermal Systems, *Transport in Porous Media*, *82*(1), 173-196.
Stock, S. (2009), *Microcomputed Tomography: Methodology and Application*, CRC Press, Boca Raton, FL.
Tokunaga, T. K. (2012), DLVO-Based Estimates of Adsorbed Water Film Thicknesses in Geologic CO_2 Reservoirs, *Langmuir*, *28*(21), 8001-8009.
Tomutsa, L., et al. (2007), Analysis of Chalk Petrophysical Properties By Means of Submicron-Scale Pore Imaging and Modeling, *SPE Reservoir Evaluation & Engineering*, *10*(3), 285-293.
Wilson, J. L. (1994), Visualization of Flow and Transport at the Pore Level, paper presented at International Symposium on Transport and Reactive Processes in Aquifers, A.A. Balkema, Rotterdam, Zurich, Switzerland, 11-15 April, 1994.

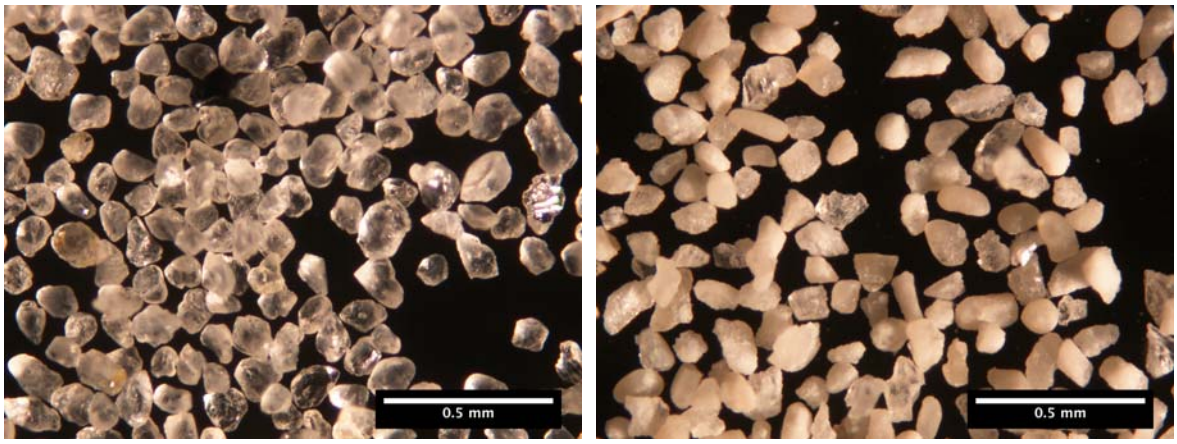

a. b.

Figure 1. Silica (a.) and calcite (b.) sand grains at the same magnification.

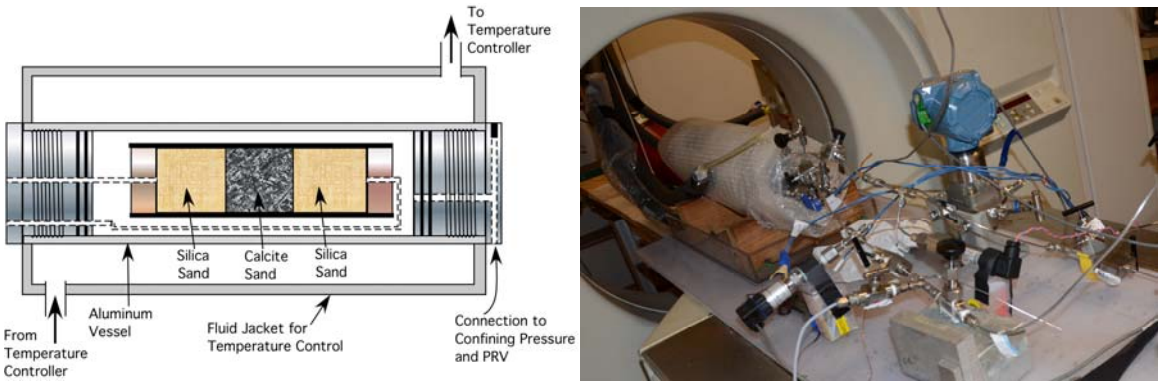

Figure 2. Experiment schematic and setup.

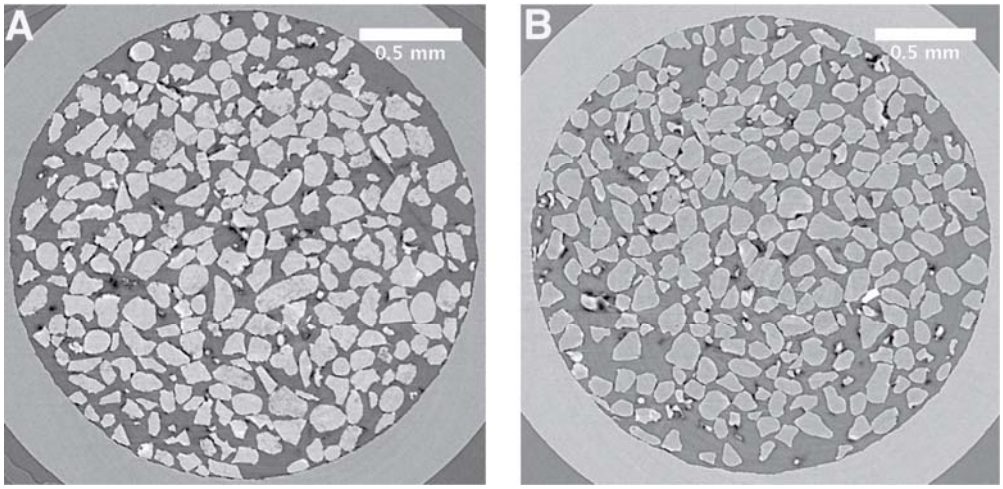

Figure 3. Slices from MicroCT image volumes acquired for the calcite sand (A) and silica sand (B).

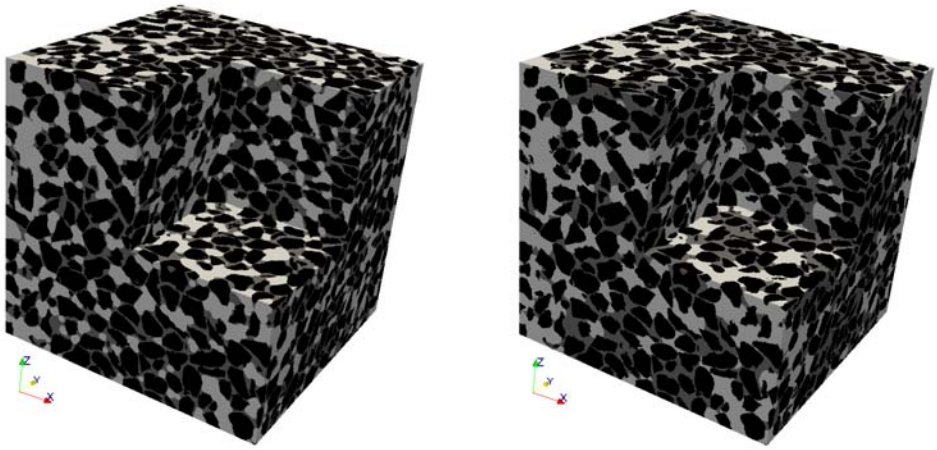

(a) (b)

Figure 4. MicroCT results and computed gas and brine capillary equilibrium for contact angles of (a) 0 and (b) 60 degrees. Brine saturation in both cases is near 48 %.

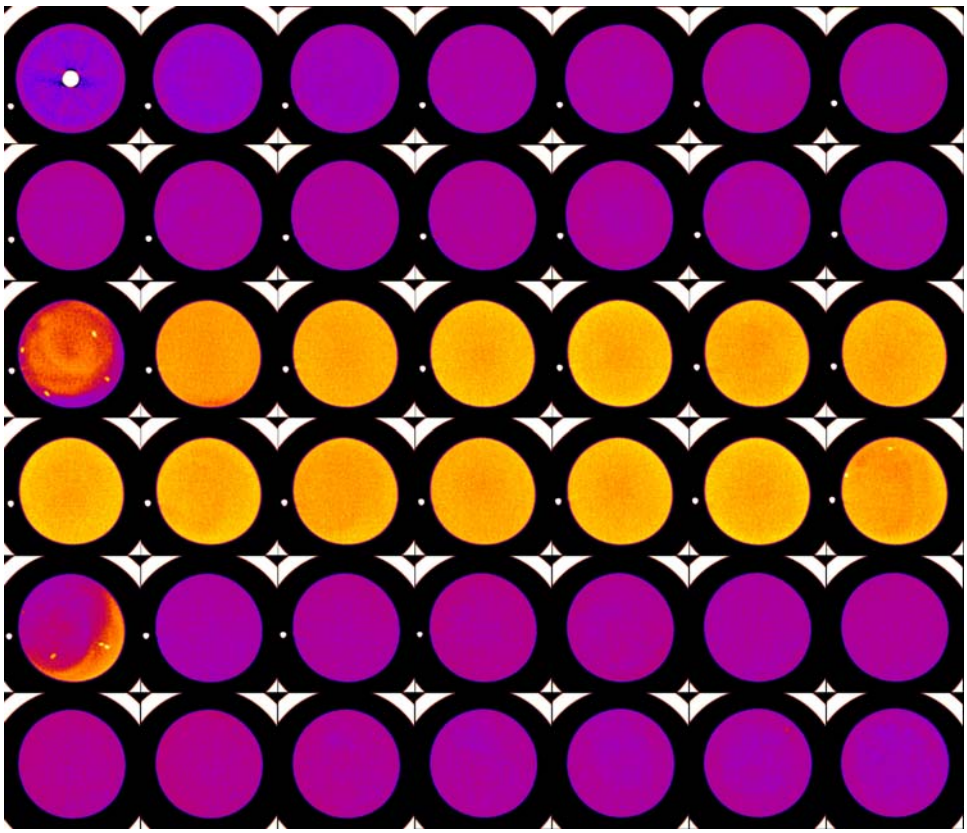

a.

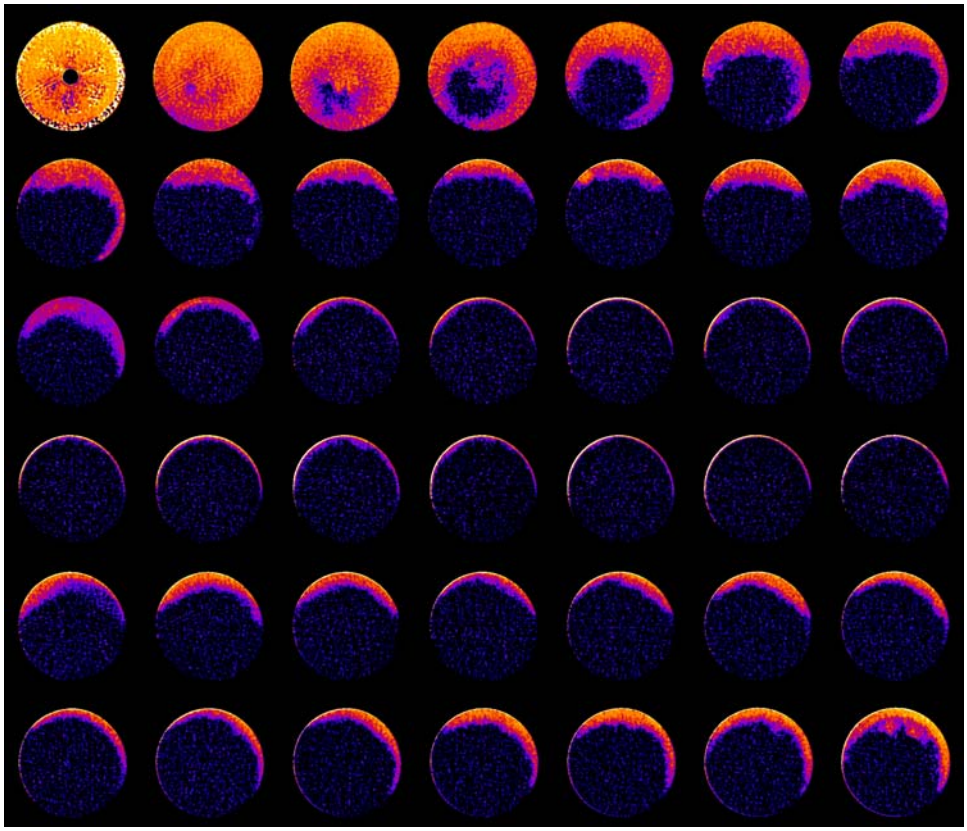

b.

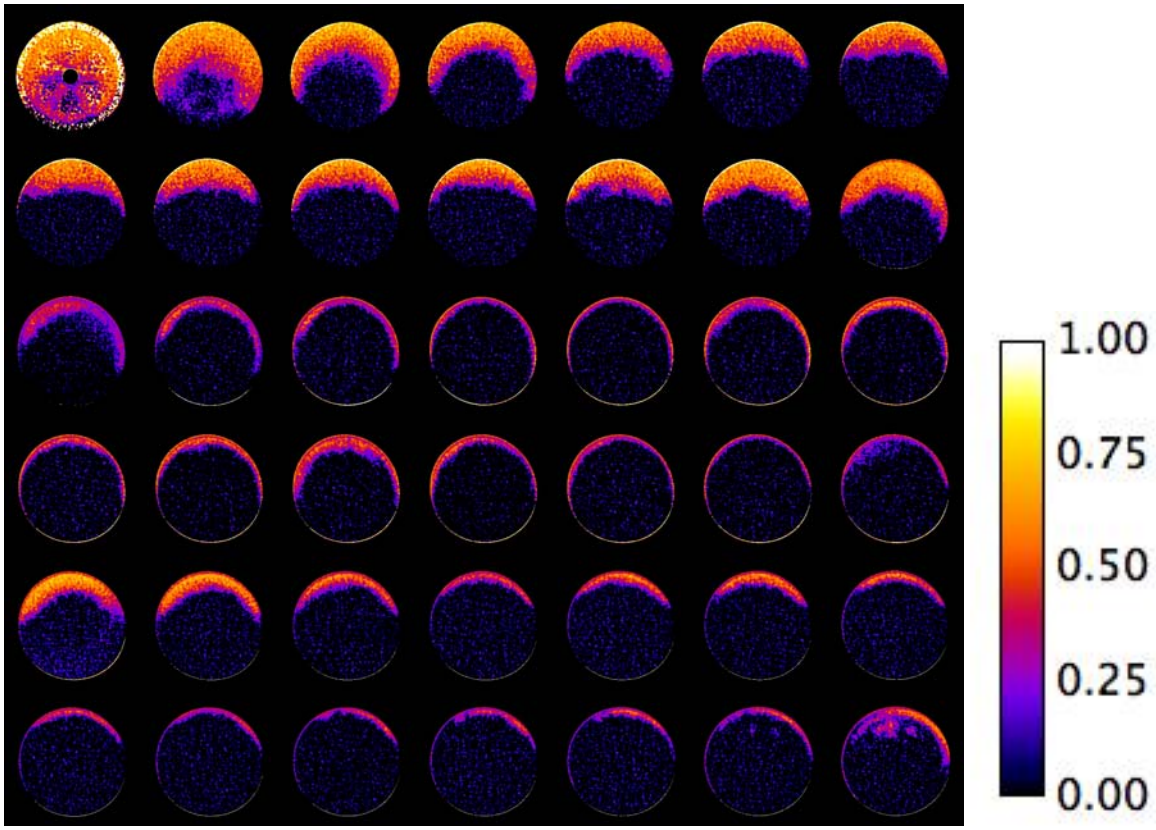

c.
Figure 5 (a.) Map of slices of the sample, silica sand is purple, calcite sand is yellow – note first slice in third and fifth rows transition between minerals; nitrogen (b.) and CO_2 (c.) saturation upon breakthrough

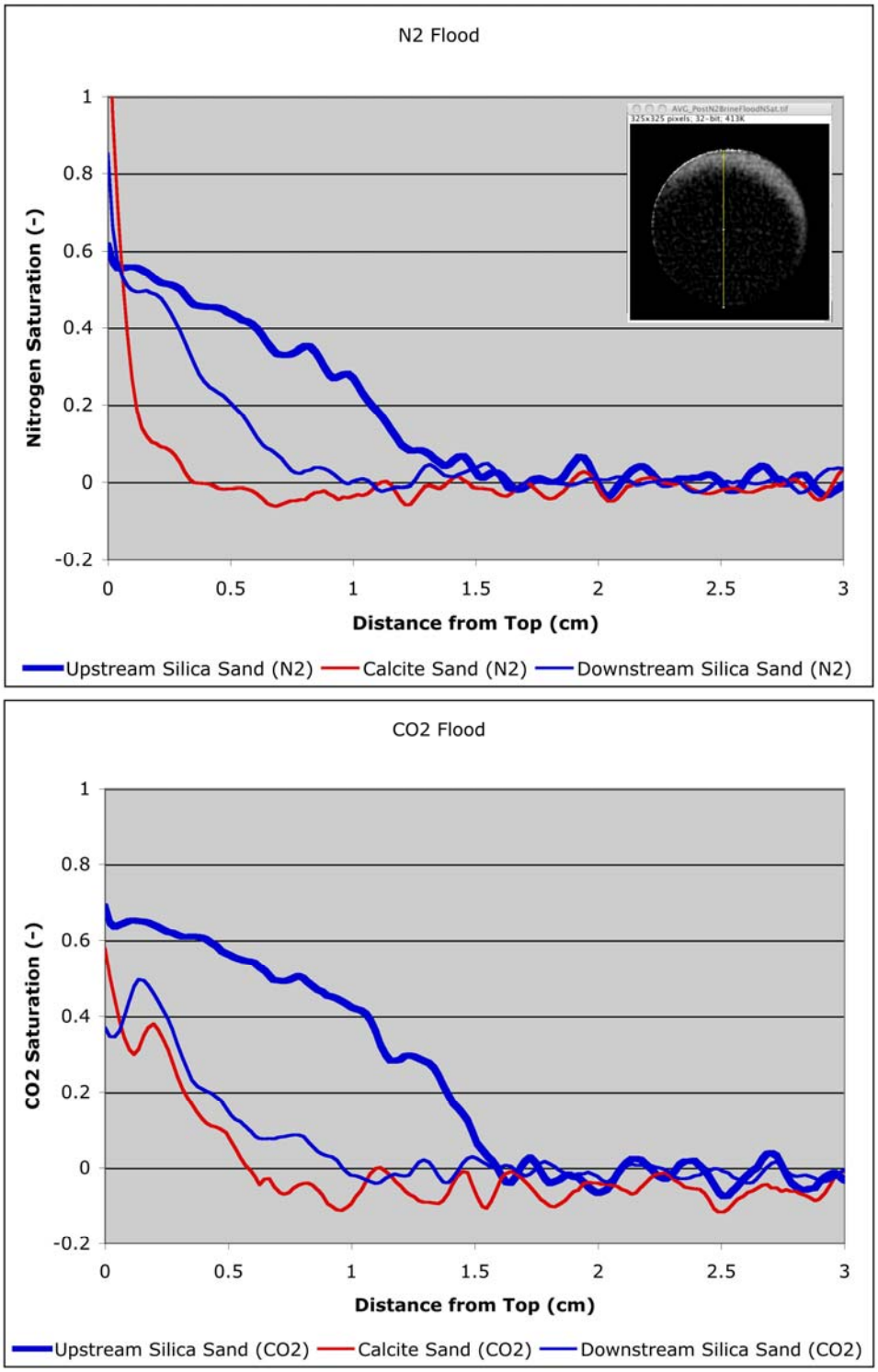

Figure 6. Nitrogen (a.) and CO_2 (b.) saturation profiles from the top of the sample.

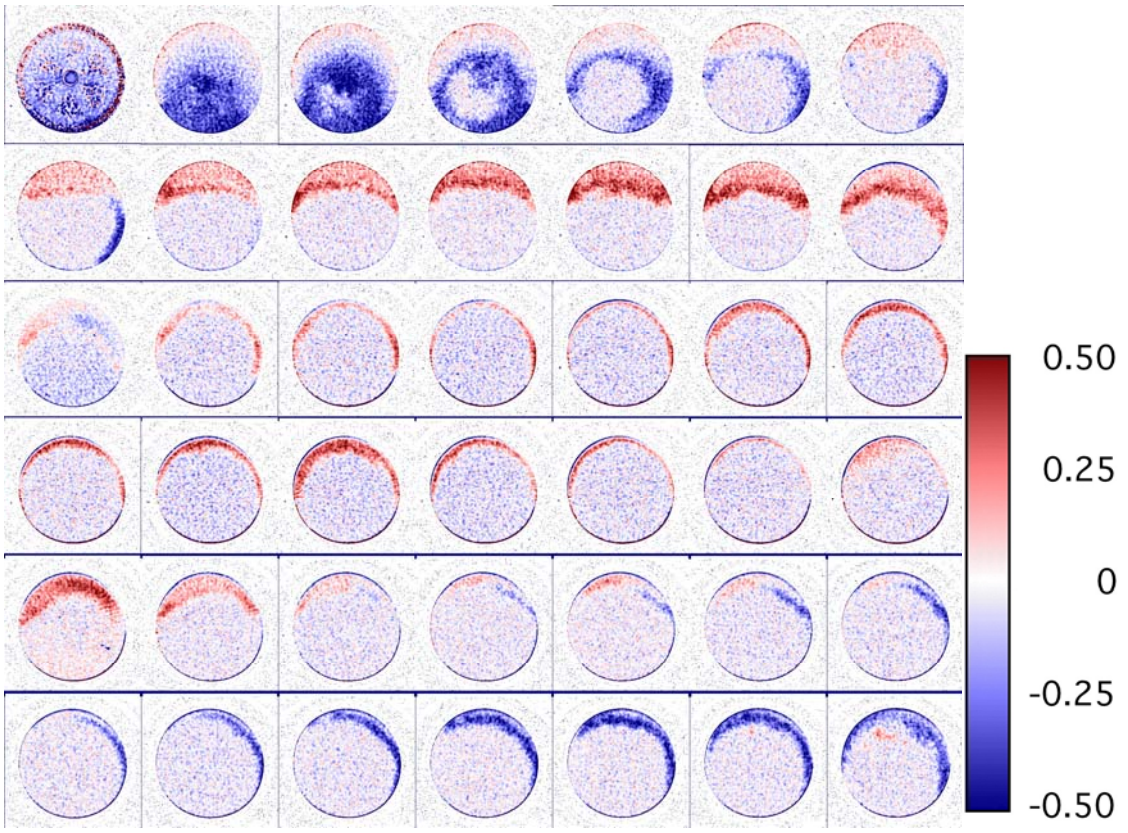

Figure 7. Difference between CO_2 and nitrogen saturation distributions at breakthrough (Figure 5b subtracted from Figure 5c). Red color indicates CO_2 saturation exceeding nitrogen saturation and blue indicates nitrogen saturation exceeding CO_2.

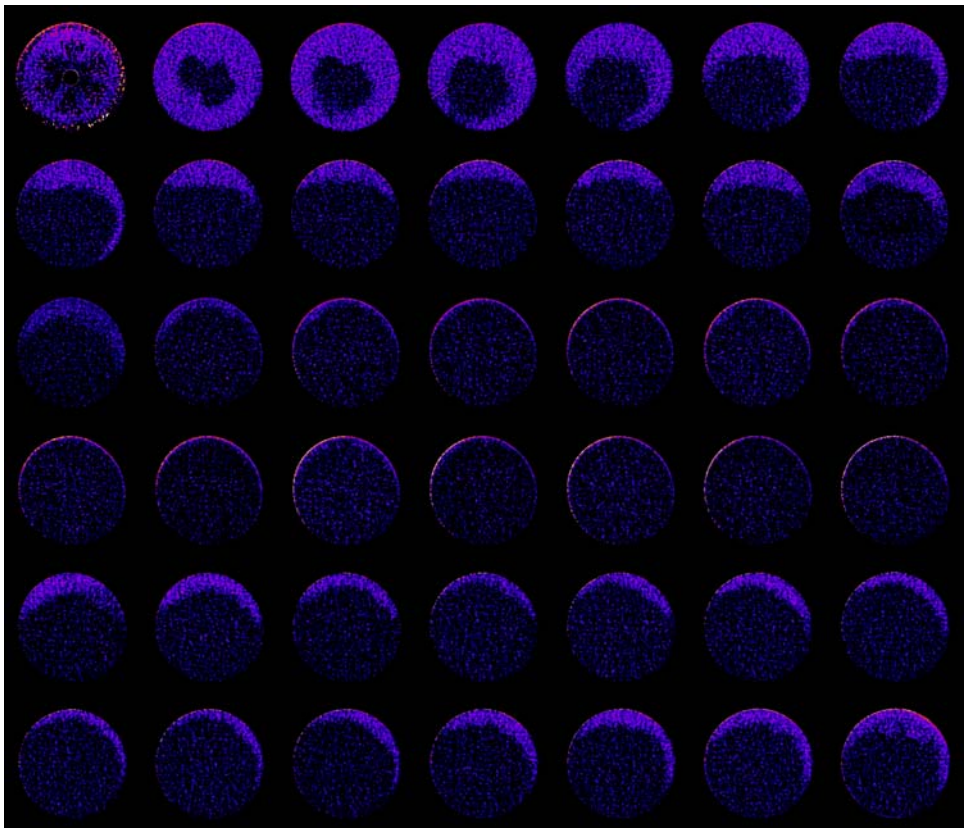

a.

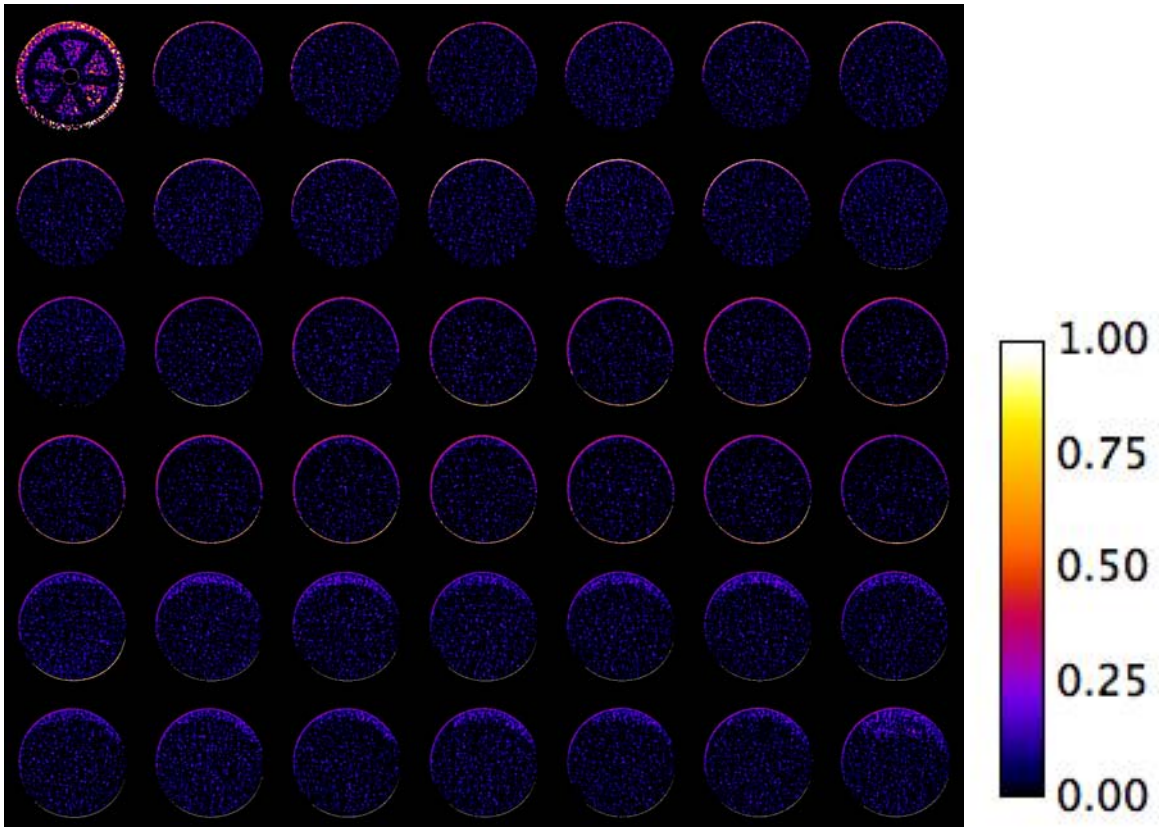

b.

Figure 8. Nitrogen (a.) and CO_2 (b.) saturations following an approximately 2 pore volume brine flood.

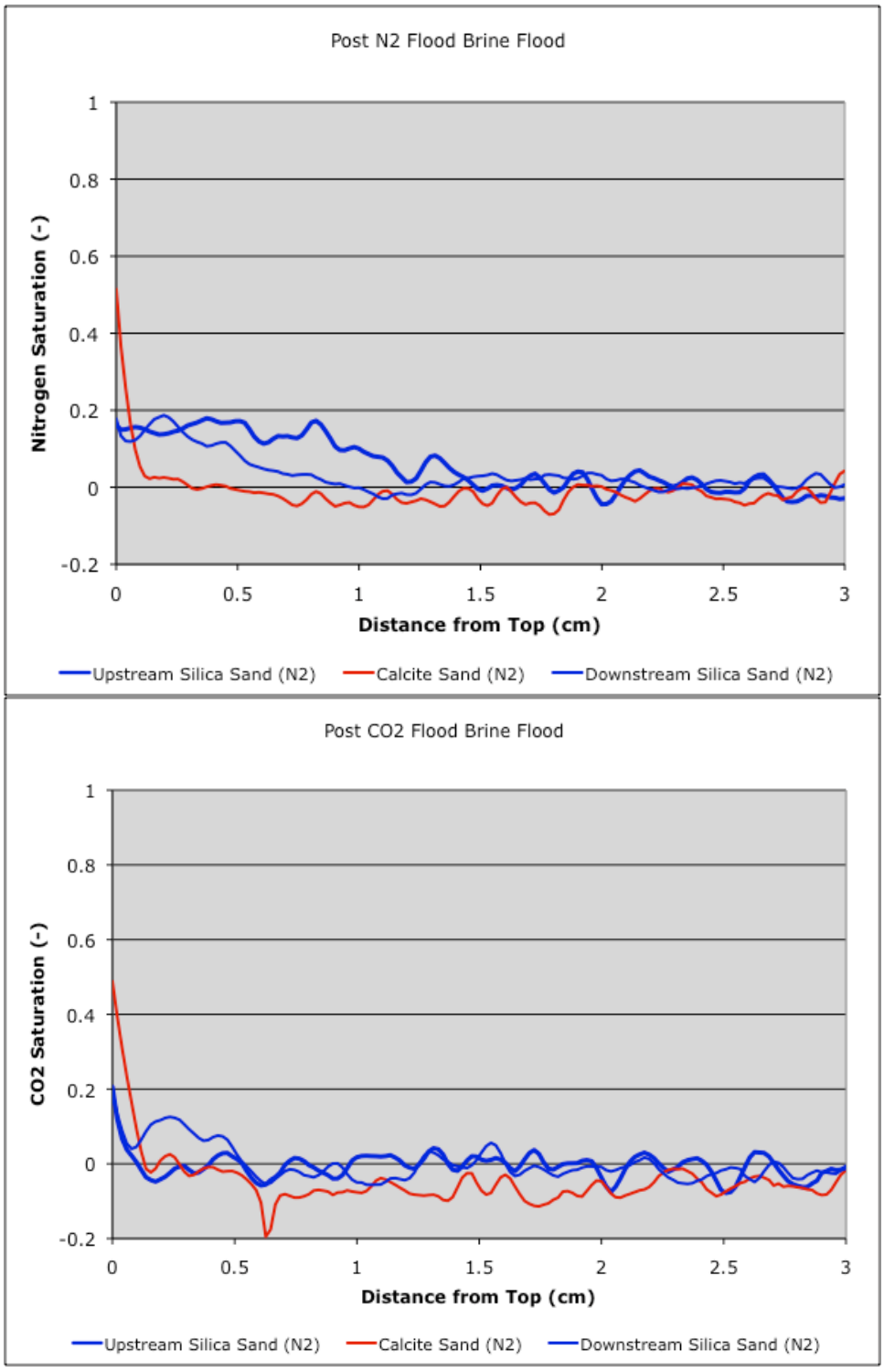

Figure 9. Nitrogen (a.) and CO_2 (b.) saturations following ~ 2 pore volume brine floods.

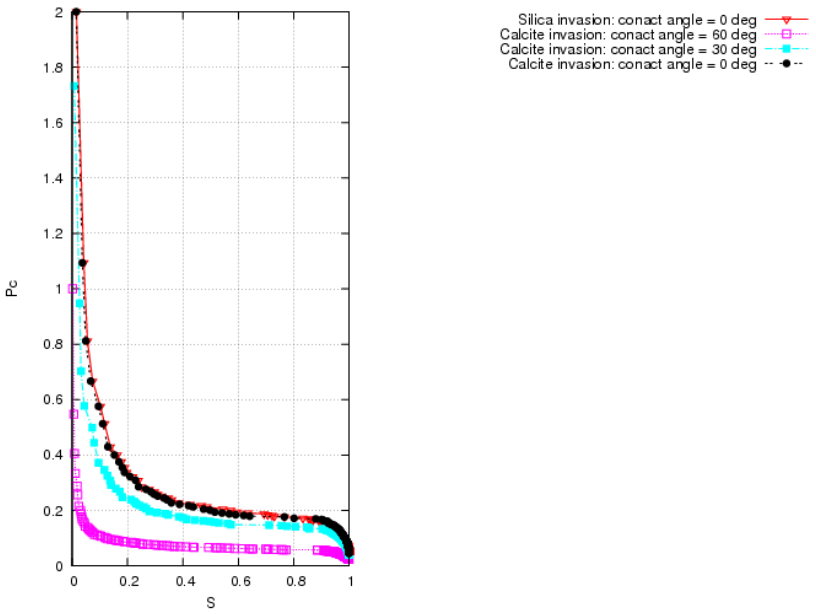

Figure 10. MIS evaluated dimensionless invasion capillary pressure curves for calcite and silica sand packs.

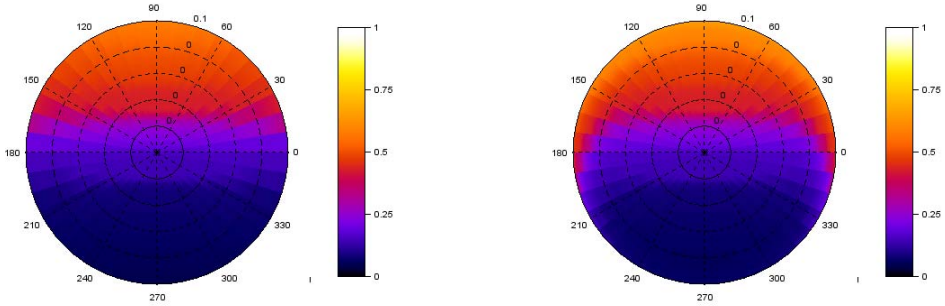

(a) (b)

Figure 11 Computed saturation profiles in the core: (a) with $f(r)=1$ (b) $f(r)$ defined by Eq. (5)

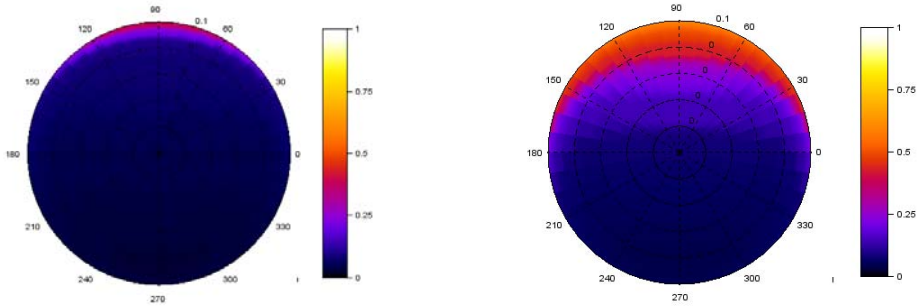

(a) (b)

Figure 12. Computed saturation distribution in the core for contact angles of (a) 0 and (b) 20 degrees.